MNE 20 (2023) 100220

Contents lists available at ScienceDirect

Micro and Nano Engineering

journal homepage: www.sciencedirect.com/journal/micro-and-nano-engineering

Detachable three-layer Au absorber microfabrication for low-temperature detectors

Jawad Hadid [a,b], Matias Rodrigues [c], Abdelmounaim Harouri [a], Christophe Dupuis [a], David Bouville [a], Antoine Martin [a], Martin Loidl [c], Laurence Ferlazzo [a,*]

[a] Centre de Nanosciences et de Nanotechnologies (C2N), CNRS, Université Paris-Saclay, F-91120 Palaiseau, France
[b] Imec vzw, Kapeldreef 75, B-3001 Leuven, Belgium
[c] Université Paris-Saclay, CEA, List, Laboratoire National Henri Becquerel (LNE-LNHB), F-91120 Palaiseau, France

ARTICLE INFO

Keywords:
Metallic magnetic calorimeters
Nanoporous surface
Gold nanofoam
Low-temperature detectors
Absorber
Electrodeposition

ABSTRACT

Low temperature detectors (LTDs) used for decay energy spectrometry (DES) can provide accurate and reliable decay data thanks to their high-energy resolution and a near 100% detection efficiency for the radiations of interest. However, it is essential to consider the source quality to mitigate spectral distortion due to the self-absorption of particle energy in the source deposited.

This work aimed to produce a replaceable 4π 3-layer gold absorber for DES in reusable metallic magnetic calorimeters, a class of LTDs. We present a novel 3-layer microfabrication process for a 1 mm diameter absorber with a total gold thickness ranging from 20 μm to 120 μm depending on the measured radionuclide (^{55}Fe or ^{241}Am). The absorber integrates a gold nanofoam in which the radionuclide is deposited by nanodrop deposition of a few tenths of μL of a radioactive solution. We fabricated a high quality gold nanofoam layer with controllable porosity through a dealloying process using wet etching and integrating it on a thick electrodeposited gold layer. The fine study of the nanofoam microfabrication is performed using high-resolution scanning electron microscopy (SEM) and energy dispersive x-ray spectroscopy (EDX).

1. Introduction

Parameters describing the decay of radionuclides, such as branching ratios, beta shape factors or particle energies, are fundamental in nuclear medicine, fuel cycle and ionizing radiation metrology. Establishing precise decay data of radionuclides is a challenge both experimentally and theoretically. The theory still needs experimental data for validation, in particular at low energy [1–3]. Due to their extremely low energy thresholds, high-energy resolution and versatility with all decays, low temperature detectors (LTDs), more precisely metallic magnetic calorimeters (MMCs) are suited to this application [4–8]. LTDs enclosing a radioactive source in their absorber can be designed to reach100% detection efficiency while maintaining a high-energy resolution and a low energy threshold [9,10]. Although LTDs can provide intrinsically a high-energy resolution, the energy spectrum can be distorted depending on the source quality embedded in the absorber; the distortion is due to self-absorption of particle energy in the source deposited and its bad thermalization with the absorber material.

In radionuclide metrology, a 4π measurement scheme with a metal absorber has been suggested using an MMC as the temperature sensor [6,11,12]. When the radionuclides are totally enclosed in a metal absorber, the energy transferred to the absorber from a decay event (for example alpha- and beta-decaying radionuclides) is converted into thermal energy. The energy released can be measured with great accuracy by the calorimeter as a temperature elevation. In order to achieve a detection efficiency of nearly 100%, the source must be surrounded by enough material to absorb the radiation of interest. The thickness of the absorber is optimized by Monte Carlo simulations according to the radiations and the energies emitted by the radionuclide. The fabrication of the absorber requires materials of high purity, a good chemical stability and a high thermal conductivity, this is the reason why gold (Au) is used. Gold has also the advantage of having a large atomic number and a large density, providing high detection efficiency.

In recent years, improvements in MMC detector microfabrication and performance for DES have been carried out by focusing on source/absorber preparation to increase the control and the reproducibility of

* Corresponding author.
E-mail address: laurence.ferlazzo@c2n.upsaclay.fr (L. Ferlazzo).

https://doi.org/10.1016/j.mne.2023.100220
Received 15 December 2022; Received in revised form 27 June 2023; Accepted 8 July 2023
Available online 10 July 2023

the locally deposited activity distribution of the source. Techniques by radioactive ion implantation [10,13] drop deposition of radioactive solutions [12,14,15], and electrodeposition [16] have been developed to enclose the radioactive source in MMC absorbers. The ion implantation gives the best source quality generating no artifacts in the spectrum, however this method is complex to use as a routine source preparation, while drop deposition is very simple but provides random source quality that should be optimized [13,14].

The quality of the source obtained by drop deposition is improved by incorporating an Au nanofoam on the first Au layer of the absorber. The Au nanofoam is encapsulated by diffusion-welding with a second Au layer [12,14]. This process has been studied to reduce the thickness of the radioactive deposit after drying the solution because of a larger effective surface. This would lead to a more homogeneous response of the detector. Previous studies of drop deposition of radionuclides on nanofoams has shown promising results: these were obtained by dealloying an electron beam evaporated Au—Ag alloy for ^{163}Ho [17] or by dealloying a rolled Au—Ag foil for ^{241}Am [14].

Furthermore, in typical fabrication processes of MMCs enclosing the source, the absorbers are strongly attached to the sensor by gluing or by microfabrication making them a single entity which cannot be dissociated [13,14]. Therefore, the MMC is limited to the measurement of only one source. Detachable absorber thermally connected to the sensor give more freedom and make MMCs re-usable.

The objective of this work is to fabricate absorbers with an integrated nanofoam on the bottom metal layer of a 4π absorber for ^{55}Fe or ^{241}Am radionuclide solutions. The goal is to integrate sources as thin as possible to mitigate spectrum shape distortion and to achieve reproducible high thermal conductivities at low temperatures. Early work showed promising results, but the integrity of the nanofoam had to be improved, mainly by reducing fabrication-induced cracks [14]. We present a reproducible microfabrication process for detachable Au absorbers in the context of reusable MMC sensors: the absorber and its source are fabricated and assembled independently from the rest of the MMC; the absorber is thermally connected to the sensor via gold wires (Fig. 1) [12]. This work establishes a novel three-layer microfabrication process of detachable 1 mm diameter Au absorbers that could be easily incorporated into other microcomponents of reusable MMCs as indicated in Fig. 1. This newly developed method to fabricate the top and bottom layers by electrolytic techniques reduces the usual imperfections often present in processing noble material foils. Au residue evaporated during laser cutting forms a critical deformation for encapsulation [15].

2. Materials and methods

2.1. Absorber design and fabrication process

The absorbers of the present work consist of up to four steps of fabrication: a bottom metal layer, a nanostructured layer (nanofoam) where the radioactive solution will be dried and a top metal foil layer (Fig. 1). The bottom and top metal layers are made of gold deposited by electroplating. The design of the device is shown in Fig. 1. The thicknesses of the bottom and top layers are 10 μm and 60 μm for absorbers with ^{55}Fe and with ^{241}Am respectively. The absorber thicknesses are to be optimized by Monte Carlo simulations of the detection efficiency depending the decay data of the specific radionuclides. The diameter of the absorber is 1 mm sufficient to deposit the solutions and to have the absorber heat capacity close to that of the MMC sensors.

The absorber processing includes several steps of microfabrication (UV and laser lithography, Physical Vapour Deposition (PVD), electroplating, wet etching and Reactive Ion Etching (RIE) as shown on Fig. 2 and detailed in the following sections of the paper.

2.2. Bottom and top gold layer fabrication (electroplating)

The bottom and top layers are manufactured using standard UV lithography and electroplating on 2-in. Si wafers. A resist was used to fabricate a mold for electroplating. A negative photosensitive resist layer was first deposited on top of a homogeneous metallic Au—Ti layer used as a seed layer for electroplating. As the target thickness for the bottom and top layers is up to 60 μm for optimized detection efficiency, thick resist had to be deposited. The KMPR1035 resist, a high contrast epoxy-based photoresist from Kayaku Advanced Material, was suited for this purpose and adapted to electroplating. The resist was then exposed to ultraviolet-UV radiation through optical masks, presenting opaque circular areas and a circular edge all around the 2-in. substrate. This Au circular edge enables to establish a uniform electrical contact for electroplating, leading to uniform and reproducible Au thicknesses for the absorber. Both bottom and top layers are circular with the same 1 mm diameter. All the size parameters were defined by a modelization of the

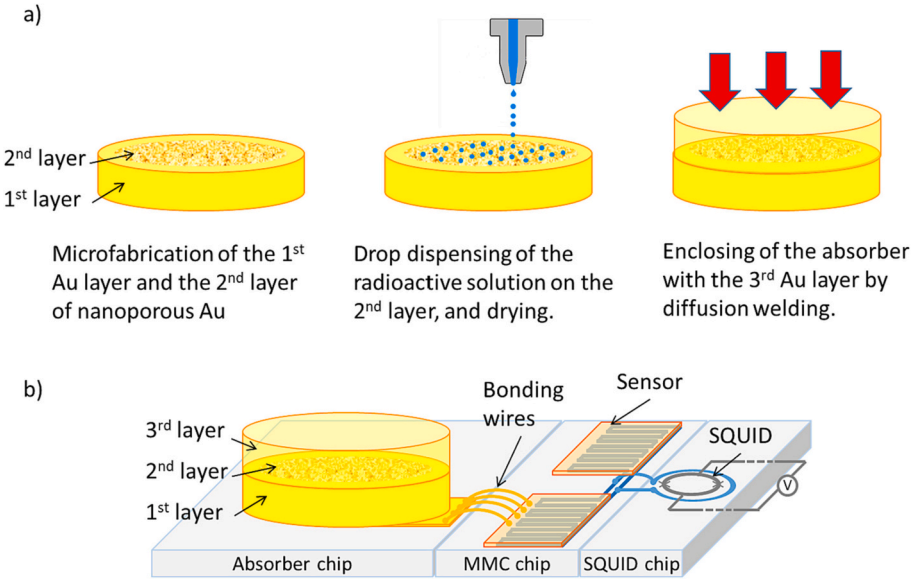

Fig. 1. (a) Scheme of process to enclose the source with the 3-layers absorbers. (b) the absorber is attached and thermally details to the MMC sensor using gold bonding wires. The signal of the paramagnetic sensor is read-out using a superconducting flux transformer (blue coils) and a DC SQUID. (For interpretation of the references to colour in this figure legend, the reader is referred to the web version of this article.)

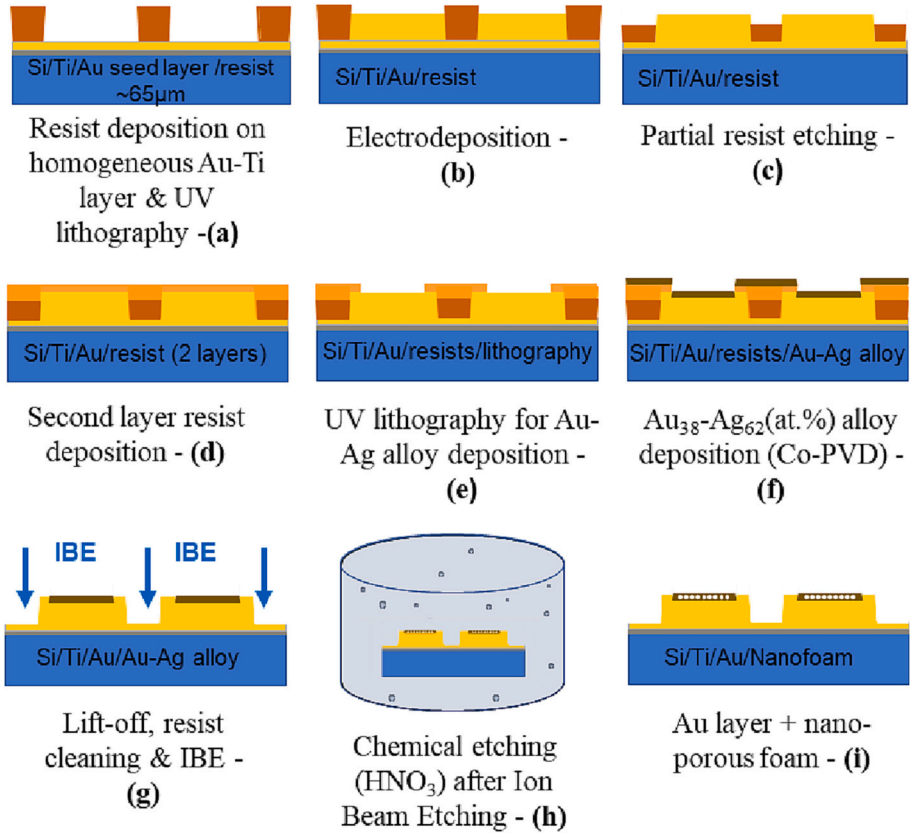

Fig. 2. Fabrication steps for the 3-layer Au absorber.

absorber aiming for the highest absorption. The top and bottom layers were prepared separately on two different 2-in. wafers presenting 12 patterns each.

The patterns were then revealed in a developer (AZ326 MIF), resulting in mask patterns reproduction on the sample. For the realization of a device, these steps must be repeated many times, with a very high accuracy of alignment between each level. In our case an accurate alignment has been done to integrate the nanofoam in the centre of the thick bottom gold layer. Electroplating has been processed in a reactor composed of a beaker, a Yamamoto substrate holder and Yamamoto stirrer. A hotplate has been used for heating the electrolytic solution toward ~60 °C. Ametek VersaStat potentiostat in a chronoamperometry mode has been utilized to precisely control the Au electroplating.

2.3. Electrolytes and thermal properties of gold electroplated

In order to achieve high-energy resolution, the electroplated gold absorber of the MMC must have a high thermal conductivity at low temperature, which is equivalent to high electrical conductivity, given the Wiedemann –Franz law. Residual Resistivity Ratio (RRR) is a commonly used measurement to characterize purity and quality of metallic sample [18]. More precisely, for a specific material, it represents the ratio of its electrical resistance R at room temperature to that at 4.2 K, $R(T = 300\ \mathrm{K})/R(T = 4.2\ \mathrm{K})$. Since the resistivity of the metal $r(T)$ depends on the contribution of the impurities (r_{imp}), on the crystalline state (r_{cryst}) associated to density of grain joint as well as dislocations, and on the phonon interaction (r_{ph}) [$r(T) \sim r_{imp} + r_{cryst} + r_{ph}(T)$]. At low temperature (4.2 K) this resistivity will be defined only by contribution of impurities and crystalline state ($r_{ph} \sim 0\ \Omega.m$).

The electrical conductivity of our absorbers was optimized by studying RRR of several electrodeposited structures fabricated using two different gold sulfite bathes (Gold-SF from Metakem and Techni Gold 25 ES RTU from Technic), using various electroplating conditions. RRR measurements can be implemented following optimized structures [19]. In our study they have been proceeded on Au meanders fabricated on SiO_2/Si substrates (Fig. 3-a). The obtained results showed in Fig. 3-b clearly indicate that Technic 25 bath has a higher RRR than the Gold-SF bath hence a better quality. This ratio increases further at higher temperature deposition (60–70 °C) and at thicker SiO_2 insulation layer (240 nm) of high dielectric strength.

2.4. Gold nanofoam fabrication

Metallic nanofoams are network structures formed by nanometric pores surrounded by interconnected ligaments. Due to their main characteristics, such as high specific surface area, very low density, high ductility and nano-architecture properties, these structures have a broad variety of applications, including catalysts [20] or fuel cells [21]. The high specific surface area and reactivity confer an interest in nanoporous surface for sensor field nanodevices [22]. For example, gas detection is achievable by the change of electrical resistivity with the species concentration and by the change of optical response due to the refractive index variation. Another important use is the incorporation of miniaturized nanofoams for medical purposes [23].

Our study aims to improve the deposit quality of the radioactive source in MMC absorbers. Acting like a sponge, the noble-metal nanofoams will be used to deposit and dry the radionuclide solution in the absorber. This will minimize the deposited source thickness and therefore, it will reduce the loss of particles energy in the deposit. Furthermore, the control and the reproducibility of the local activity distribution onto absorbers will also be improved. These developed gold nanofoam layers will be used for drop depositing and drying a few tenths of µL of ^{55}Fe and ^{241}Am radioactive solutions. The solution is deposited by a nanodrop dispenser system spraying drops of few tens µm diameter on the nanofoam surface.

Selective dissolution of alloyed materials [24] and template methods

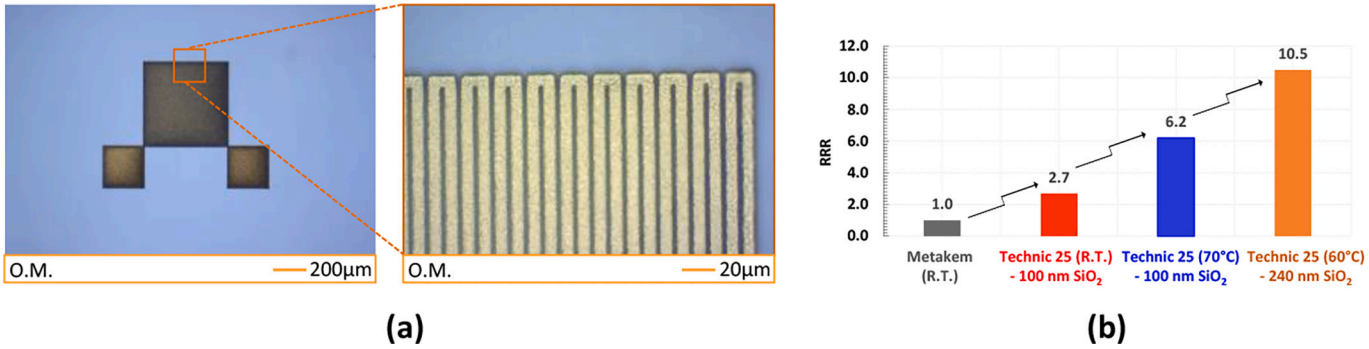

Fig. 3. (a)-Au meander for RRR measurements. (b)-Residual resistivity measurements (RRR) for 2 different Au sulfite electroplating baths kept at Room Temperature (RT) or higher temperature during the process.

[25] producing random distributed and organized nanostructures respectively, are the common techniques used for developing metallic nanofoams. For our microfabrication process the alloying-dealloying technique was adopted with the dissolution of the less noble metal in a co-sputtered two metals alloy. RF/DC cathodic co-sputtering Alliance Concept AC450 equipment was used for alloy deposition. For the fabrication of the Au nanofoam we chosed to dealloy the Au—Ag metal couple. We aimed to set the fraction of the non-noble (Ag) metal about 60 at.% accordingly to literature [24] in order to be close to the parting limit of the Au—Ag alloy system; it should reduce the residual tension in the nanoporous layer and the presence of cracks. Although high temperature annealing is supposed to suppress volume shrinkage hence cracks formation [24] for this first microfabrication process, no pre-annealing was realized. EDX coupled to a Magellan XL400 SEM was used to analyse dealloying process. The average area of the pore at each etching time was evaluated using the high-resolution SEM images and ImageJ software [26,27] the public domain image processing program developed by the National Institutes of Health and the LOCI laboratory University of Wisconsin. An example of s SEM image of the nanofoam surface after dealloying as well as its exploitation using ImageJ is shown in Fig. 4. We can clearly notice that the nanofoam forms an interconnected network of ligaments and pores (Fig. 4-a), but also that image processing (Fig. 4-b) and SEM image (Fig. 4-a) images match well.

2.5. Nanofoam integration in the 3-layer absorber

The integration of the nanofoam on the top of the bottom layer of the absorber was realized by a double UV lithography as described in Fig. 2. The first one presented in the part *2.1* (using a 70 µm thick KMPR1035 resist) allowed the 60 µm thick bottom layer electroplating (Fig. 2-a-b). The second UV lithography (using a 3 µm thick nLof resist) was aligned on the first one, the disk is centred on the bottom layer (Fig. 2-d-e). For a better fit between the two resist layers which is promoted by a flattened topography, an O_2 plasma etching (using a Nanoplas asher equipment) of the top of KMPR1035 resist down to the Au layer level and slightly below was realized (Fig. 2-c).Then, the Au—Ag layer was co-sputtered and lifted off by stripping both resist layers in a single step (Fig. 2-f-g). Dealloying of Ag was carried out to form the Au nanofoam after dry etching the Ti—Au seed layer using a Roth&Rau ion beam etching equipment (Fig. 2-h). This process has been developed to integrate a 0.8 mm diameter nanofoam on the 1 mm diameter Au bottom layer following the modelization recommendations to have the best coupling (PrimA-LTD project[1]).

[1] The PrimA-LTD project aims to develop new measurement techniques to determine the activity as well as fundamental nuclear data and measurement of beta shape spectrum using low temperature detectors https://prima-ltd.net/ .

3. Results and discussion

3.1. Bottom and top gold layer

The uniform Au electroplating deposition has successfully resulted in the creation of 1 mm thick Au top layers, as shown in Fig. 5. These layers are effectively separated from the Si substrate by utilizing a HF + HNO_3 solution, which acts as a wet etching agent [28], completely removing the substrate. The bottom layers of the absorber consist of 60 µm thick Au pads, which are deposited using the same process and host the nanofoam layer. The separated top layers are then utilized as caps for the nanofoam. To ensure a secure attachment to the bottom layer, a diffusion welding technique is employed, involving pressing and heating the layers at 400 °C. This step is vital for sealing the source once the ^{55}Fe or ^{241}Am radionuclide is deposited onto the nanofoam and subsequently dried.

3.2. Au nanofoam

Au—Ag alloy was co-deposited with 38–62 at. % respectively. For dealloying, HNO_3 (initial concentration of 68%) was used with two different dilutions and temperatures.

Figs. 6 and 7 present the results obtained for Ag etching by using HNO_3 at 50 °C and 100 °C with a dilution of 17% and 50% respectively. The deposited layer, showing Au—Ag grains on Fig. 6-a, was dealloyed by HNO_3 solution creating the small pores and ligaments observed in Fig. 6-b. When the etching time is increased to 17 h, pores and ligaments size increased continuously (Fig. 6-c) with no cracks detection (Fig. 6-d). EDX analyses show that in the case of low HNO_3 concentration and low temperature, etching requires more than 17 h for a total dealloying (~0% Ag left). For higher temperature and higher concentration of acid the etching duration decreases toward 2 h without forming any cracks in the Au nanofoam.

When the HNO_3 concentration and the temperature are increased to 50% and 100 °C, the dealloying duration decreases from 17 toward 2 h (Fig. 8-blue curve) with no crack occurrence (Fig. 7). The pores (Fig. 7) seem to be more connected with longer ligaments than in the first conditions (Fig. 6). Thermal treatment, clearly play an important role in increasing pores size. Moreover, the results show that the porosity can then be tunable by playing on these parameters (solution concentration, temperature, etching time) according to the nanofoam application.

Based on previous theoretical work on nanofoam, we know that the appearance of porosity during dealloying is due to the dynamically formed structure during the etching process and is not due to the simple excavation of one phase from a two-phase microstructure. The first studies carried out by Forty [29] showed that noble atoms could migrate. Erlebacher et al. [30,31] have presented an analytical atomistic model that clarified the underlying physics of porosity evolution during dealloying. The model involves an interfacial phase separation in which

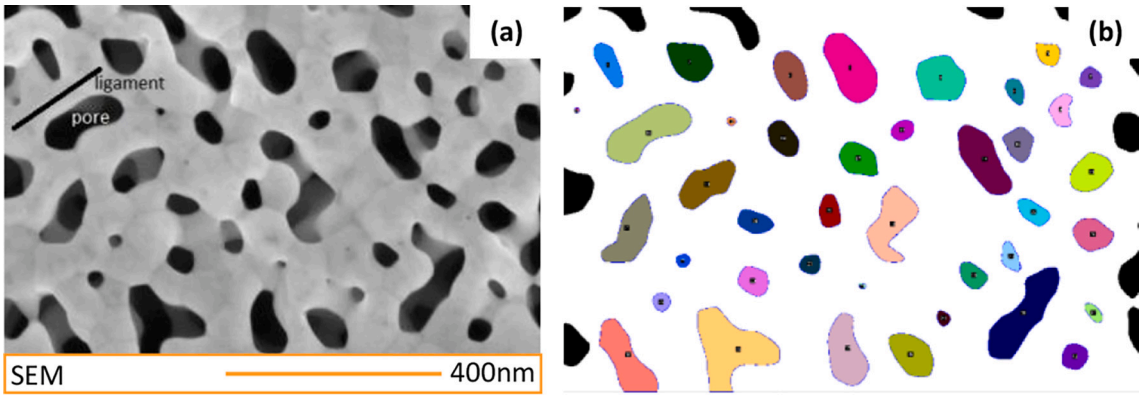

Fig. 4. Nanofoam after etching during 10 h with HNO_3 (17% dilution at 50 °C) (a)-SEM image (b)- ImageJ image processing.

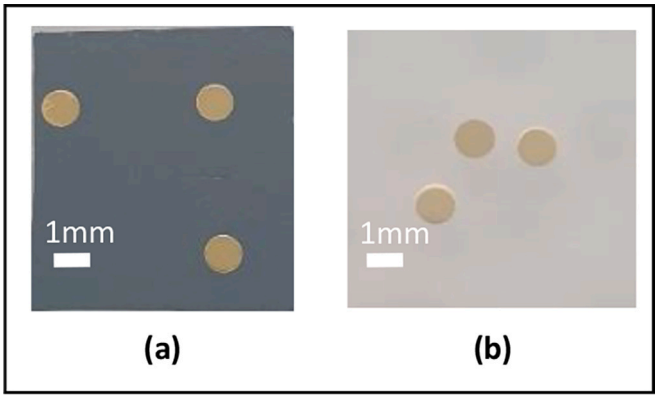

Fig. 5. Optical microscopy image for the 1 mm diameter top Au layers (enclosure layer) (a)-before and (b)-after separation from Si substrate.

gold atoms not dissolved from the alloy/electrolyte interface tend to cluster and form islands, rather than uniformly distribute themselves over the surface which would passivate the interface and stop further etching. This process continuously opens up regions in virgin alloy, and allows the dissolution front to penetrate through the bulk of the material. Controlling dealloying can lead to porous solids with macroscale dimensions. The large surface-to-volume ratio and the bicontinuous structure provide transport pathways to lead to dealloying under the control of an electric or chemical potential [32].

EDX analysis shows an exponential decrease of the Ag at. % concentration with etching time (Fig. 8-red & blue curve) while the average area of the pores at the surface, measured using ImageJ processing, increases linearly and continuously even after the almost total Ag dealloying (Fig. 8-green curve). On the contrary, the total area of the pores at the surface reaches a threshold (Fig. 9). These results are in good agreement with theory showing a clustering of the noble atoms during the dealloying leading to pore size increase. The porosity can be thus adjustable depending upon the dealloying time and conditions.

The SEM cross section image (Fig. 10-b), shows that the dealloying is homogeneous down to the interface with the underlying layer and highlights an inter-connected pore structure. A relationship seems to exist between the uniform porosity in the bulk of the nanofoam and the initial concentration of Ag. To reach a uniform porosity in the bulk of the nanofoam, we need high concentration of Ag (~60 at. %) to have percolation of several groups of atoms that means a continuity of this

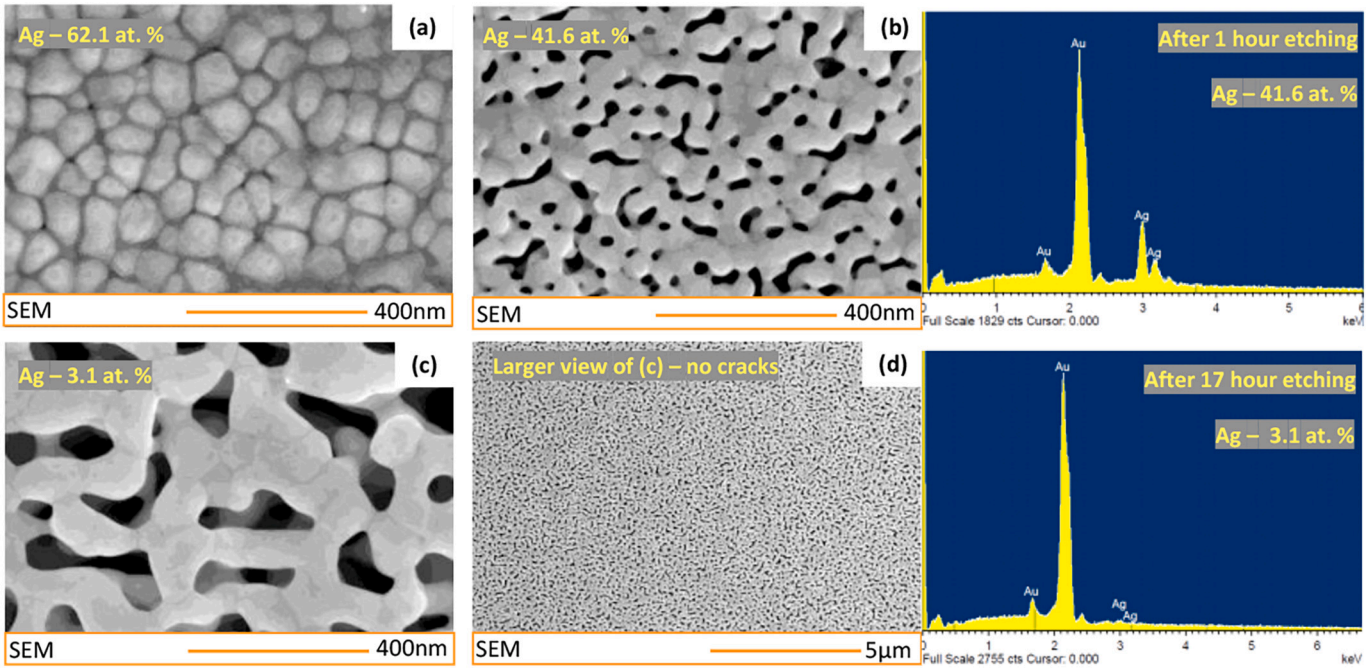

Fig. 6. Nanofoam fabrication: with HNO_3 (17% dilution at 50 °C).

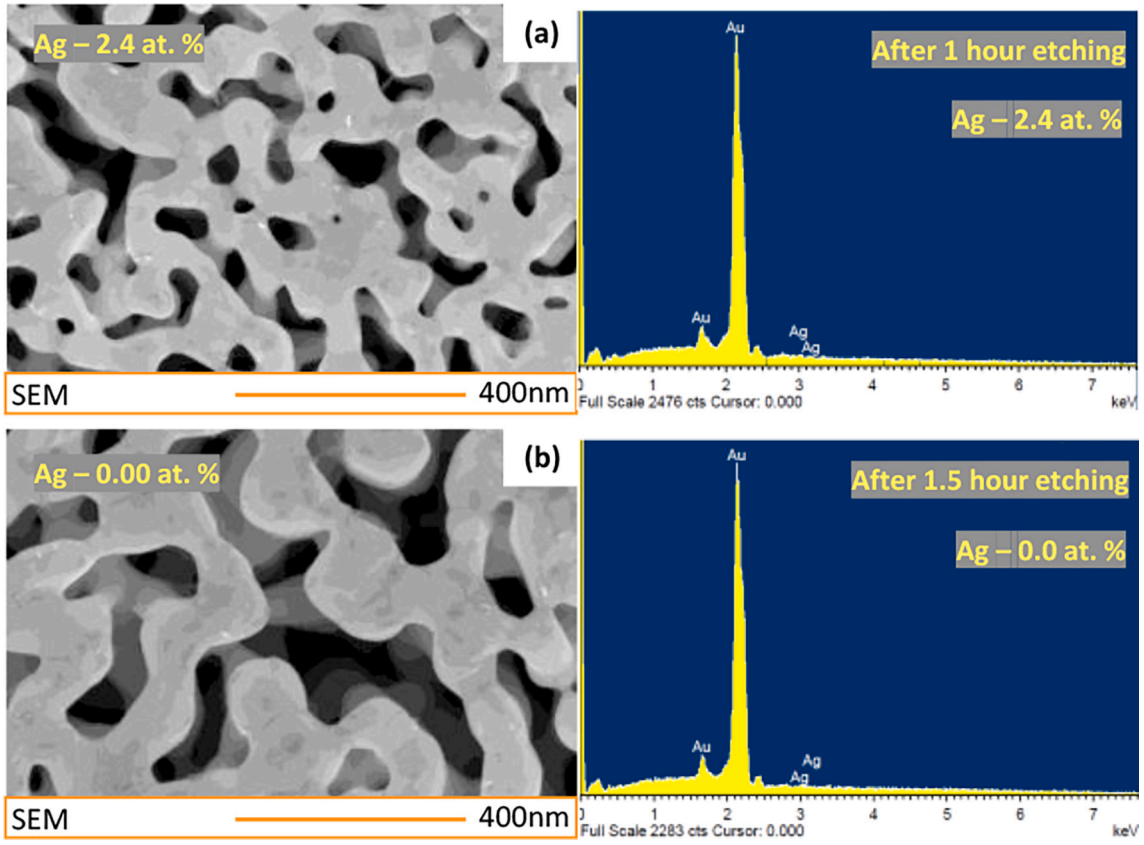

Fig. 7. Nanofoam fabrication: HNO_3 (50% dilution at 100 °C).

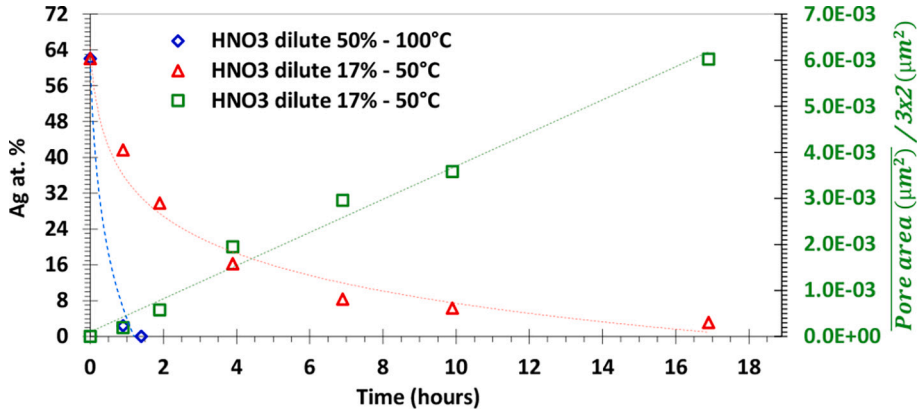

Fig. 8. Ag at.% and average pore area as a function of time etching for different temperatures and different HNO_3 concentrations.

element from the surface to the interface with the gold layer below. In this case, there will be a critical value of x ($Au_{1-x}Ag_x$) below which dealloying will not succeed.

The nanofoam integrated to the absorber (Fig. 11) can be then capped with the 3rd Au layer by diffusion welding, after ^{55}Fe or ^{241}Am radionuclide drop deposition (Fig. 1).

4. Conclusion

This work introduces a novel microfabrication process forming three Au layers, which integrates the middle Au nanofoam between the top and bottom absorber layers. This 3-layer Au structure can be easily connected to the sensor, enabling the reusability of MMC. The authors have fabricated the top and bottom layers using electrolytic techniques, thereby reducing the typical imperfections observed when machining noble foils. In addition, they have successfully implemented a gold nanofoam on the bottom Au layer, which exhibits tunable porosity. This feature enables to minimize the thickness of the source layer and therefore reduce the absorption of particles energy in the deposit which is responsible for the spectrum distortion. The fine study of the nanofoam microfabrication has been performed using high-resolution scanning electron microscopy (SEM) and energetic dispersive x-ray spectroscopy (EDX).

Declaration of Competing Interest

The authors declare that they have no known competing financial interests or personal relationships that could have appeared to influence

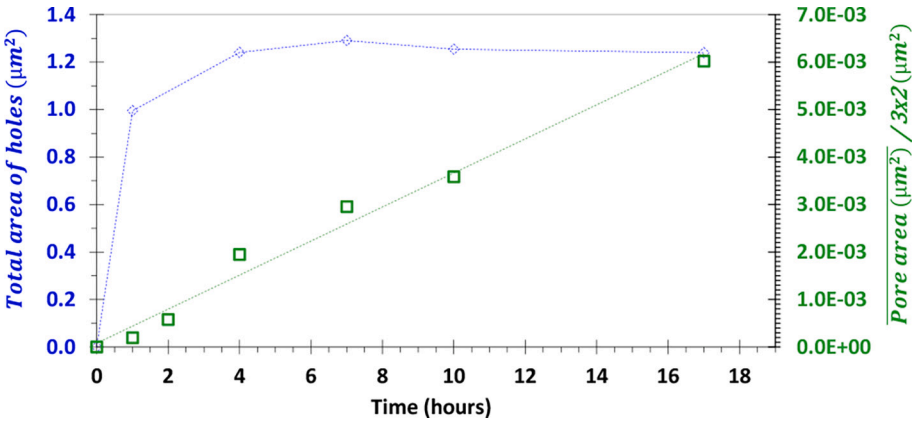

Fig. 9. Total area and average area of pores at the nanofoam surface as a function of etching time.

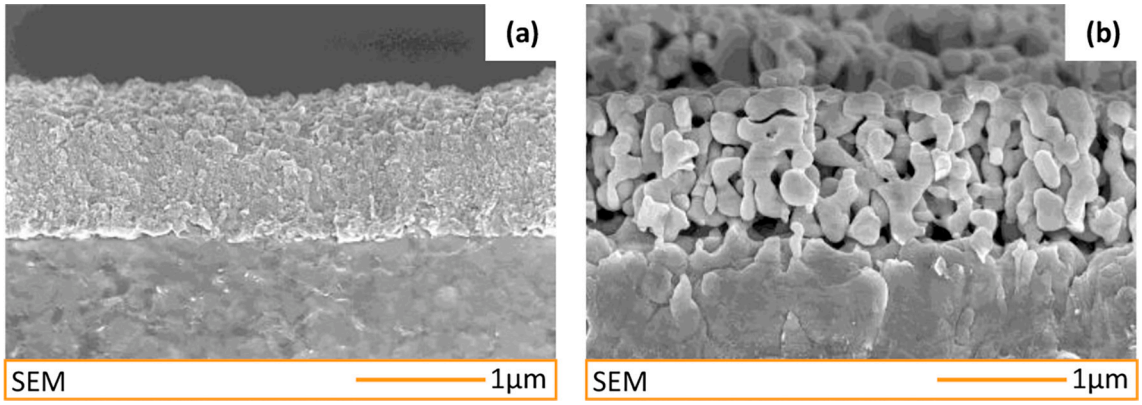

Fig. 10. Cross section of the (a)- the as deposited Au—Ag layer and (b)-Au nanofoam after dealloying lying on the electroplated 1st Au layer of the absorber.

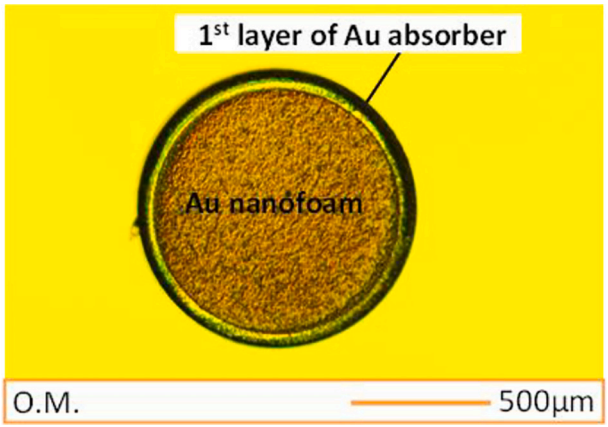

Fig. 11. Optical image for 0.8 mm diameter Au nanofoam integrated on the bottom layer of the 1 mm diameter Au absorber.

the work reported in this paper.

Data availability

Data will be made available on request.

Acknowledgments

This work is part of the project 20FUN04 PrimA-LTD that has received funding from the EMPIR programme co-financed by the Participating States and from the European Union's Horizon 2020 research and innovation programme. This work was done within the C2N micro nanotechnologies platforms and was partly supported by the RENATECH network and the General Council of Essonne. The authors thank Laetitia Leroy for PVD deposition, Sebastian Kempf and Joern Beyer for fruitful discussion in the choice of Au electrolyte.

References

[1] X. Mougeot, Towards high-precision calculation of electron capture decays, Appl. Radiat. Isot. 154 (2019), 108884.
[2] K. Kossert, M. Loidl, X. Mougeot, M. Paulsen, P. Ranitzsch, M. Rodrigues, High precision measurement of the ^{151}Sm beta decay by means of a metallic magnetic calorimeter, Appl. Radiat. Isot. 185 (2022), 110237.
[3] M. Braß, M.W. Haverkort, Ab initio calculation of the electron capture spectrum of 163Ho: Auger–Meitner decay into continuum states, New J. Phys. 22 (2020), 093018.
[4] H. Rotzinger, M. Linck, A. Burck, M. Rodrigues, M. Loidl, E. Leblanc, L. Fleischmann, A. Fleischmann, C. Enss, Beta spectrometry with magnetic calorimeters, J. Low Temp. Phys. 151 (2008) 1087–1093.
[5] M. Loidl, M. Rodrigues, B. Censier, S. Kowalski, X. Mougeot, P. Cassette, T. Branger, D. Lacour, First measurement of the beta spectrum of ^{241}Pu with a cryogenic detector, Appl. Radiat. Isot. 68 (2010) 1454–1458.
[6] M. Loidl, M. Rodrigues, C. Le-Bret, X. Mougeot, Beta spectrometry with metallic magnetic calorimeters, Appl. Radiat. Isot. 87 (2014) 302–305.
[7] S. Kempf, A. Fleischmann, L. Gastaldo, C. Enss, Physics and applications of metallic magnetic calorimeters, J. Low Temp. Phys. 193 (2018) 365–379.
[8] K.E. Koehler, Low temperature microcalorimeters for decay energy spectroscopy, Appl. Sci. 11 (2021) 4044.
[9] P.C.-O. Ranitzsch, C. Hassel, M. Wegner, D. Hengstler, S. Kempf, A. Fleischmann, C. Enss, L. Gastaldo, A. Herlert, K. Johnston, Characterization of the ^{163}Ho electron capture spectrum: a step towards the electron neutrino mass determination, Phys. Rev. Lett. 119 (2017), 122501.
[10] C. Velte, F. Ahrens, A. Barth, K. Blaum, M. Braß, M. Door, H. Dorrer, Ch. E. Düllmann, S. Eliseev, C. Enss, P. Filianin, A. Fleischmann, L. Gastaldo, A. Goeggelmann, T. Day Goodacre, M.W. Haverkort, D. Hengstler, J. Jochum, K. Johnston, M. Keller, S. Kempf, T. Kieck, C.M. König, U. Köster, K. Kromer,

F. Mantegazzini, B. Marsh, Yu.N. Novikov, F. Piquemal, C. Riccio, D. Richter, A. Rischka, S. Rothe, R.X. Schüssler, Ch. Schweiger, T. Stora, M. Wegner, K. Wendt, M. Zampaolo, High-resolution and low-background ^{163}Ho spectrum: interpretation of the resonance tails, Eur. Phys. J. C. 79 (1026) (2019) 1–8.

[11] S.J. Lee, M.K. Lee, Y.S. Jang, I.H. Kim, S.K. Kim, J.S. Lee, K.B. Lee, Y.H. Lee, Y. H. Kim, Cryogenic measurement of alpha decay in a 4π absorber, J. Phys. G Nucl. Part. Phys. 37 (2010) 055103.

[12] Y.S. Jang, S.J. Lee, G.B. Kim, I.H. Kim, M.S. Kim, H.J. Lee, J.S. Lee, K.B. Lee, M. K. Lee, H.C. Ri, et al., Development of decay energy spectroscopy for radionuclide analysis using cryogenic 4π measurements, J. Low Temp. Phys. 167 (2012) 967–972.

[13] F. Mantegazzini, A. Barth, H. Dorrer, Ch.E. Düllmann, C. Enss, A. Fleischmann, R. Hammann, S. Kempf, T. Kieck, N. Kovac, C. Velte, M. Wegner, K. Wendt, T. Wickenhäuser, L. Gastaldo, Metallic magnetic calorimeter arrays for the first phase of the ECHo experiment, Nuclear Inst. and Methods in Physics Research, A 1030 (2022), 166406.

[14] M. Rodrigues, M. Laarraj, M. Loidl, X.-F. Navick, L. Ferlazzo, Preparation of drop-deposited sources in 4π absorbers for total decay energy spectrometryJ, Low Temp. Phys. 199 (2020) 461–466.

[15] L. Bockhorn, M. Paulsen, J. Beyer, K. Kossert, M. Loidl, O.J. Nähle, P.C.-O. Ranitzsch, M. Rodrigues, Improved source/absorber preparation for radionuclide spectrometry based on low-temperature calorimetric detectors, J. Low Temp. Phys. 199 (2020) 298–305.

[16] M. Rodrigues, M. Laarraj, M. Loidl, M., et al., Development of total decay energy spectrometry of α-emitting radionuclides using metallic magnetic calorimeters, J. Low Temp. Phys. 193 (2018) 1263–1268.

[17] M.P. Croce, M.W. Rabin, V. Mocko, G.J. Kunde, E.R. Birnbaum, E.M. Bond, J. W. Engle, A.S. Hoover, F.M. Nortier, A.D. Pollington, W.A. Taylor, N.R. Weisse-Bernstein, L.E. Wolfsberg, J.P. Hays-Wehle, D.R. Schmidt, D.S. Swetz, N. Ullom, T. E. Barnhart, R.J. Nickles, Development of holmium-163 electron-capture spectroscopy with transition-edge sensors, J. Low Temp. Phys. 184 (2016) 958.

[18] G.T. Meaden, Electrical Resistance of Metals 89, Heywood Books, London, 1965.

[19] F. Blondelle, A. Sultan, E. Collin, H. Godfrin, Electrical conductance of bolted copper joints for cryogenic applications, J. Low Temp. Phys. 175 (3/4) (2014) 1.

[20] R. Song, J. Han, M. Okugawa, R. Belosludov, T. Wada, J. Jiang, D. Wei, A. Kudo, Y. Tian, M. Chen, H. Kato, Ultrafine nanoporous intermetallic catalysts by high-temperature liquid metal dealloying for electrochemical hydrogen production, Nature Communications 13 (2022) 5157.

[21] Y. Kang, J. Wang, Y. Wei, Y. Wu, D. Xia, L. Gan, Engineering nanoporous and solid core-shell architectures of low-platinum alloy catalysts for high power density PEM fuel cells, Nano Res. 15 (7) (2022) 6148–6155.

[22] Xu Pengcheng, Xinxin Li, Haitao Yu, Tiegang Xu, Advanced nanoporous materials for micro-gravimetric sensing to trace-level bio/chemical molecules, Sensors 14 (2014) 19023.

[23] A. Hashmi, V. Nayak, K.R.B. Singh, B. Jain, M. Baid, F. Alexis, A.K. Singh, Potentialities of graphene and its allied derivatives to combat against SARS-CoV-2 infection, Materials Today Advances 13 (2022) 100208.

[24] E. Seker, M.L. Reed, M.R. Begley, A thermal treatment approach to reduce microscale void formation in blanket nanoporous gold films, Scr. Mater. 60 (2009) 435–438.

[25] R.-H. Zhu, H.-B. Wang, T.-T. Xue, D.-J. Zeng, Y.-Z. Xing, L. Zhou, D.-Y. Ma, Biomass template method for preparing macroporous nickel foam with tunable pore size and porosity, Mater. Lett. 323 (2022) 132540.

[26] W.S. Rasband, U.S. ImageJ, National Institutes of Health, Bethesda, Maryland, USA. https://imagej.nih.gov/ij/, 1997-2018.

[27] C. Schneider, W. Rasband, K. Eliceiri, NIH image to image J: 25 years of image analysis, Nat. Methods (2012) 671–675.

[28] T.E. Burgess, Chemical etching of germanium in HF-HNO_3-H_2O solutions, J. Electrochem. Soc. (1962) 341–342.

[29] A.J. Forty, Corrosion micro-morphology of noble-metal alloys and depletion gilding, Nature 282 (1979) 597–598.

[30] J. Erlebacher, M.J. Aziz, A. Karma, N. Dimitrov, K. Sieradzki, Evolution of nanoporosity in dealloying, Nature 410 (2001) 450–452.

[31] J. Erlebacher, An atomistic description of dealloying - porosity evolution, the critical potential, and rate-limiting behavior, J. Electrochem. Soc. 151 (2004) 614–626.

[32] J. Weissmüller, K. Sieradzki, Dealloyed nanoporous materials with interface controlled behaviour, MRS Bull. 43 (2018) 14–19.